

Sensitivity of the Acoustic Scattering Problem in Prolate Spheroidal Geometry with Respect to Wavenumber and Shape

D. Kourounis, L.N. Gergidis, and A. Charalambopoulos¹

Abstract: The sensitivity of analytical solutions of the direct acoustic scattering problem in prolate spheroidal geometry on the wavenumber and shape, is extensively investigated in this work. Using the well known Vekua transformation and the complete set of radiating “outwards” eigensolutions of the Helmholtz equation, introduced in our previous work ([Charalambopoulos and Dassios (2002)], [Gergidis, Kourounis, Mavratzas, and Charalambopoulos (2007)]), the scattered field is expanded in terms of it, detouring so the standard spheroidal wave functions along with their inherent numerical deficiencies. An approach is employed for the determination of the expansion coefficients, which is optimal in the sense, that minimizes the L^2 norm of the error related to the satisfaction of the boundary condition on the surface of the scatterer. The study of the conditioning of the matrices involved in the linear systems, the solution of which provides the expansion coefficients, reveals the need for implication of numerical implementations using arbitrary precision arithmetics. Numerical and convergence properties estimations such as condition numbers, L^2 and L^∞ error norms prove the robustness of the adopted methodology. A study of the dependence of the error with respect to geometrical, physical and numerical parameters is developed. Three dimensional representation of the L^2 norm clarifies the distribution of errors on the scatterer’s surface.

Keyword: Prolate Spheroid; Acoustic Scattering; Vekua Transformation; Arbitrary Precision; L^2 -norm Minimization; Mathematical Modeling; Numerical Acoustics; Scientific Computing.

1 Introduction

The investigation of the scattering problem in spheroidal geometry has attracted the scientific interest for several decades. This is of course due to the simplicity and the important property of the spheroidal system to fit quite accurately to several geometrical configurations, lacking symmetry only in one Cartesian direction and simulating successfully a large variety of inclusions or inhomogeneities participating in scattering processes. A lot of effort has been devoted especially in the realm of time harmonic acoustics to study the direct scattering problem by spheroids. The adopted methodology depends crucially on the frequency range under consideration.

In the resonance region, the most popular approaches employ either separation of variables or T-matrix methods [Waterman (1969)], [He, Xie, and Ye (1997)], [Varadan and Varadan (1982)], [Hackman (1984)]. In the vast majority of these approaches, the well known spheroidal wave functions dominate, which emerge via the spectral analysis of Helmholtz equation in spheroidal coordinates. These functions are constructed via a necessary intermediate numerical scheme, which becomes cumbersome and extremely complicated for spheroids with large focal distances and small semi axes ratio. In addition, the spheroidal wave functions are defined via infinite expansions in terms of basis functions of separable form and the convergence becomes poor in the upper limit of the resonance region and even worse in the high frequency realm. Particularly for high frequencies, the only practical recourse is to resort to asymptotic methods (e.g. ray tracing). These methods, on the other hand, are not error-controllable since they solve an approximate model instead of the original equations (e.g. the

¹ Department of Materials Science and Engineering, University of Ioannina, GR 45110 Ioannina, Greece

eikonal equation instead of the Helmholtz equation itself). The adoption of resonance techniques in the high frequency regime, in cases that this is realizable, increases severely the computational resources. For instance, the Mie theory for acoustic scattering from a sphere of radius a , predicts that the number of summation terms, is proportional to $k^2a + c(ka)^{1/3} + b^2$ (k is the wavenumber and c, b suitable constants) as the frequency becomes higher [Wang, Wu, He, and L.Li (2005)]. This is the reason why traditionally, the Sommerfeld-Watson transformation is used to change the summation into a residue series.

It is prominent so, that there are several numerical difficulties inherent to the solution of the scattering problem using analytical methods, strongly depended on the geometrical features of the scatterer and the imposed frequency (or equivalently the induced wave number). Apart from the intrinsic numerical difficulty in the determination of the spheroidal wave functions, the standard methodology of expanding the scattered field in terms of the aforementioned basis leads to extremely ill-conditioned matrices, involved in the linear systems derived by the boundary condition satisfaction. It is widely recognized [Bailey (2004)], [Borwein and Bailey (2004)], that the 64-bit and 80-bit IEEE floating point arithmetic formats, currently provided and utilized in most computer systems, are inadequate for the inversion of ill-conditioned matrices of this type [Trefethen and Bau (1997)]. In addition, in acoustics, there exist problems in which we need extremely accurate values for the estimation of the acoustic field. More precisely, we are frequently interested in sound pressure level predictions (*SPL*). The *SPL* factor is given by $SPL = 20 \log_{10}(|u(x)|/\sqrt{2}u_{ref})$ where u_{ref} is the usual reference pressure and $|u(x)|$ the amplitude of the acoustic field. [Chandler-Wilde (2007)]. So the accurate prediction of *SPL* requires small relative errors in the computations of $|u|$. In fact, we need very small absolute errors at points x where $|u(x)|$ is small. Such regions play a very important role in acoustics. For example, someone may be interested in accurate predictions in the shadow zone if he calculates the shielding performance of a

noise barrier. Thus very reliable numerical methods are of interest for a variety of acoustic applications such as Finite Elements, Boundary Elements [Agnantiaris and Polyzos (2003)], [Callsen, von Estorff, and Zaleski (2004)] [Qian, Han, and Atluri (2004)], [Qian, Han, Ufimtsev, and Atluri (2004)], [Tsai, Lin, Young, and Atluri (2006)], [Chen, Fu, and Zhang (2007) and Method of Moments [Chandrasekhar and Rao (2007)].

In our previous work ([Gergidis, Kourounis, Mavratzas, and Charalambopoulos (2007)]), we introduced a new theoretical setting inspired by a novel concept [Charalambopoulos and Dassiou (2002)] where the Vekua transformation is adopted [Vekua (1942)], [Vekua (1967)], [Vekua (1945)] in order to construct Helmholtz equation solutions by transforming appropriately the well known spheroidal harmonic functions. This setting detours the standard spheroidal wave functions avoiding so, all the involved therein intrinsic numerical deficiencies and truncation errors. In the present work, we extend the numerical investigation of the acoustic scattering problem from spheroidal scatterers, introduced in [Gergidis, Kourounis, Mavratzas, and Charalambopoulos (2007)] towards the high frequency regime.

In Section 2 we present the necessary theoretical outcome, taken from [Gergidis, Kourounis, Mavratzas, and Charalambopoulos (2007)]. We also provide additional theoretical arguments and justifications regarding the completeness of the constructed solution set. The scattered field emanating due to the interference of a plane acoustic wave with an impenetrable soft spheroidal scatterer is represented as an expansion in terms of the elements of the Vekua basis. This infinite expansion is truncated and forced to satisfy the boundary condition on the scatterer's surface. For the determination of the expansion coefficients we follow the L^2 error norm minimization methodology [Gergidis, Kourounis, Mavratzas, and Charalambopoulos (2007)] which has been proven very robust and reliable in the low frequency regime even for very elongated spheroidal bodies. The numerical investigation of the system, the solution of which furnishes the truncated expan-

sion coefficients and its conditioning is presented in Section 3. There we also present an extensive convergence analysis of our approach in terms of truncation level, geometry and wavenumber. Additionally we provide the global dependence of the L^2 norm of the error as a function of the aforementioned three parameters. The cornerstone of the numerical implementation is arbitrary precision facilities, [Bailey (2004), Bailey, Yozo, Li, and Thompson (2002), Wolfram Research (2004)] an indispensable tool for several scientific areas, such as Experimental Mathematics, Climate Modeling [Borwein and Bailey (2004)], Computational Geometry [Shewchuk (1997)] among many others, which in our case allows the solution of the encountered linear systems. Finally the main outcome of the direct scattering problem, i.e. the far field pattern, is constructed and appropriately visualized for indicative wave numbers ranging from the low frequency region, resonance region to the dawn of high frequency asymptotics.

It is worthwhile to notice here that relevant scattering problems involving penetrable spheroidal scatterers hosting (or not) spheroidal inclusions of arbitrary orientation are under current investigation in the framework of the present approach. It is also interesting to mention that the adoption of the new basis in combination with the L^2 norm minimization of the error on the interfaces has been proven to be an efficient combined technique, extending successfully the range of applicability of analytical methods in simple or multiple scattering problems.

2 Theoretical formulation

In [Vekua (1942, 1967)] one can find a very interesting one-to-one transformation connecting the solutions of Laplace and Helmholtz equations with regular behavior near the origin, for arbitrary space dimensions.

This connection of solution spaces gives birth to the concept of solving a dynamic interior boundary value problem involving the Helmholtz equation, by transforming, through the Vekua mapping, the solution of the corresponding static problem referring to the Laplace operator.

In spheroidal geometry, the aforementioned framework leads to the construction of interior dynamic solutions [Charalambopoulos and Dassios (2002)] constituting a basis of Helmholtz operator $\nabla^2 + k^2$ and having the following representation

$$\begin{aligned} u_{nm}(\mathbf{r}) &= \sum_{p=0}^{\lfloor \frac{n}{2} \rfloor} \sum_{l=0}^{\lfloor \frac{n-2p}{2} \rfloor} B_{n,m,p,l} \Gamma(n-2p + \frac{3}{2}) \\ &\times \frac{J_{(n-2p+\frac{1}{2})}(kr)}{(\frac{kr}{2})^{n-2p+1/2}} P_{n-2p-2l}^m(\cosh \mu) \\ &\times P_{n-2p-2l}^m(\cos \theta) e^{im\phi} \quad n = 0, 1, 2, \dots; |m| \leq n. \end{aligned} \quad (1)$$

The spheroidal coordinates (μ, θ, ϕ) are connected with the Cartesian ones through the coordinate transformations

$$\left\{ \begin{array}{ll} x = \frac{\alpha}{2} \sinh \mu \sin \theta \cos \phi & 0 \leq \mu < \infty \\ y = \frac{\alpha}{2} \sinh \mu \sin \theta \sin \phi & 0 \leq \theta \leq \pi \\ z = \frac{\alpha}{2} \cosh \mu \cos \theta & 0 \leq \phi < 2\pi \end{array} \right\} \quad (2)$$

where α stands for the focal distance. The coefficients $B_{n,m,p,l}$ have specific values, the symbol Γ stands for the well known Gamma function while the Bessel function $J_{n-2p+1/2}$ of the "dimensionless" radial distance, plays crucial role for the regularity of solutions in the vicinity of the origin.

In [Gergidis, Kourounis, Mavratzas, and Charalambopoulos (2007)], the authors extend the previous results to exterior dynamic problems describing scattering processes. The exterior solutions obtain the form

$$\begin{aligned} \hat{u}_{nm}(\mathbf{r}) &= \sum_{p=0}^{\lfloor \frac{n}{2} \rfloor} \sum_{l=0}^{\lfloor \frac{n-2p}{2} \rfloor} B_{n,m,p,l} \Gamma(n-2p + \frac{3}{2}) \\ &\times \frac{2 h_{n-2p}^{(1)}(kr)}{\sqrt{\pi} (\frac{kr}{2})^{n-2p}} \\ &\times P_{n-2p-2l}^m(\cosh \mu) P_{n-2p-2l}^m(\cos \theta) e^{im\phi}, \\ &n = 0, 1, 2, \dots; |m| \leq n. \end{aligned} \quad (3)$$

where the spherical Hankel function $h_{n-2p}^{(1)}$ has replaced the Bessel one and incorporates the outgoing propagating behavior of Helmholtz equation scattered solutions. In this section we restrict ourselves to give explicitly the proof for the completeness of the set (3). All the other theoretical

ingredients of the method appear in the aforementioned work.

We remark first that $\hat{u}_{nm} = u_{nm} + i\tilde{u}_{nm}$ where \tilde{u}_{nm} is constructed with the Bessel function of first kind in Eq.(3) replaced by the corresponding Neumann function. Let u be an arbitrary outwards radiating solution of the Helmholtz equation. Its regular part $Regu$ can be expanded in terms of the complete set u_{nm} (in the space of regular Helmholtz equation solutions) as

$$Regu = \sum_{n,m} \gamma_{nm} u_{nm}. \quad (4)$$

We define

$$w = \sum_{n,m} \gamma_{nm} \hat{u}_{nm} = Regu + i \sum_{n,m} \gamma_{nm} \tilde{u}_{nm}. \quad (5)$$

The function $u - w$ satisfies Helmholtz equation and the Sommerfeld radiation condition, while disposing zero regular part. Then

$$u - w = \frac{e^{ikr}}{r} g(\theta, \phi) + O\left(\frac{1}{r^2}\right), \quad r \rightarrow \infty, \quad (6)$$

where $g(\theta, \phi)$ is the scattering amplitude of the radiating field. Remark that

$$Reg(u - w) = i \frac{\sin(kr)}{r} g(\theta, \phi) + O\left(\frac{1}{r^2}\right) \quad (7)$$

and then $g(\theta, \phi)$ vanishes. Invoking of Relich's lemma leads to the result that $u - w$ vanishes in the whole exterior domain. Thus $u = \sum_{n,m} \gamma_{nm} \hat{u}_{nm}$, establishing completeness.

The above analysis settles the background to develop the corresponding scattering problem. We consider a prolate spheroidal acoustically impenetrable scatterer occupying a specific region in R^3 , defined by the scatterer's surface S , represented by the spheroidal surface

$$\mu = \mu_0 \quad (8)$$

The exterior region of the scatterer is denoted by D and is characterized by the range $\mu > \mu_0$, $0 \leq \theta \leq \pi$, $0 \leq \phi < 2\pi$ of spheroidal coordinates. The scatterer is illuminated by a time harmonic incident acoustic plane-wave, with frequency ω .

Suppressing the time dependence $e^{-i\omega t}$ in all the physical quantities of the scattering process, the incident field is represented by the time reduced plane wave

$$u^{inc}(\mathbf{r}) = e^{i\mathbf{k}\cdot\mathbf{r}}, \quad \mathbf{r} \in D \quad (9)$$

where $\mathbf{k} = k\hat{\mathbf{k}}$, k is the wavenumber of the process and $\hat{\mathbf{k}}$ is the direction of the incident field. The presence of the scatterer in the medium where the wave propagates, gives rise to a secondary acoustic field, the scattered one denoted by u^{sc} , which satisfies exactly as the incident wave, the Helmholtz equation. This field emanates from the scatterer and radiates to infinity, satisfying uniformly over all directions, the well known Sommerfeld radiation condition. The total field $u(\mathbf{r}) = u^{inc}(\mathbf{r}) + u^{sc}(\mathbf{r})$ defined in $\bar{D} = D \cup S$, obeys, on scatterer's surface, to a specific type of boundary condition, depending on the special nature of the scatterer. We focus on the soft scatterer case implying that

$$u(\mathbf{r}) = u^{inc}(\mathbf{r}) + u^{sc}(\mathbf{r}) = 0, \quad \mathbf{r} \in S. \quad (10)$$

We expand, the unknown scattered field in terms of the aforementioned radiating basic solutions to obtain

$$u^{sc}(\mathbf{r}) = \sum_{n=0}^{\infty} \sum_{m=-n}^n A_{nm} \hat{u}_{nm}(\mathbf{r}), \quad \mathbf{r} \in D, \quad (11)$$

where the coefficients A_{nm} absorb the unknown character of $u^{sc}(\mathbf{r})$.

The representation (11) can be exploited to provide the far-field pattern, which determines the behavior of the scattered field far-away from the scatterer and constitutes usually the measured quantity in direct scattering. The far-field region is the region, where the angular field distribution is essentially independent of distance from the scatterer. If the scatterer has a maximum overall dimension C , that is large compared to the wavelength, the far-field region is commonly taken to exist at distances greater than C^2/λ from the scatterer, λ being the wavelength. What is necessary, is to investigate the asymptotic behavior (for $r \rightarrow \infty$) of the eigensolutions $\hat{u}_{nm}(\mathbf{r})$. In the realm

of large $r \gg 1$, we apply an extended, but straightforward asymptotic analysis of the special functions involved in the definition formula of $\hat{u}_{nm}(\mathbf{r})$. Then equation (11) obtains the asymptotic form

$$u^{sc}(\mathbf{r}) = \frac{e^{ikr}}{kr} f_{\infty}(\theta, \phi) + O\left(\frac{1}{r^2}\right), \quad r \rightarrow \infty \quad (12)$$

where the far-field pattern $f_{\infty}(\theta, \phi)$ is given by

$$\begin{aligned} f_{\infty}(\theta, \phi) &= \sum_{n=0}^{\infty} \sum_{m=-n}^n \frac{2}{\sqrt{\pi}} e^{-i\frac{\pi}{4}} A_{nm} \\ &\times \sum_{p=0}^{\lfloor \frac{n}{2} \rfloor} B_{n,m,p,0} \Gamma\left(n-2p+\frac{3}{2}\right) e^{-i\frac{1}{2}(n-2p+\frac{1}{2})\pi} \\ &\times \left(\frac{4}{k\alpha}\right)^{n-2p} \\ &\times \frac{2^{2p-n} [2(n-2p)]!}{(n-2p)!(n-2p-m)!} P_{n-2p}^m(\cos\theta) e^{(im\phi)}. \end{aligned} \quad (13)$$

The satisfaction of the boundary condition (10) leads to the determination of the expansion coefficients appeared in (11) and hence to the solution of the direct scattering problem.

3 Numerical Investigation and Implementation

The numerical implementation of our approach involved both C++ and Mathematica software developing, for consistency checks. Both implementations relied heavily on arbitrary precision, without which the range of the frequency of the incident wave, the geometry and the truncation level of the series that could be handled, would be severely restricted. The need for arbitrary precision motivated the use of general computing environments like Mathematica [Wolfram Research (2004)] which incorporates arbitrary precision in a very natural way. The need for performance and convenience motivated the development of C++ software. Arbitrary precision arithmetic in C++ was provided by ARPREC library [Bailey, Yozo, Li, and Thompson (2002)]. The implementations of special functions in C++ was based on [Press, Teukolsky, Vetterling, and Flannery (2002); Zhang and Jin (1996)] with the necessary modifications and tuning to the working

precision. This involves recalculation of all the usual parameters and mathematical constants entering the definition of special functions to the desired precision and appropriate modifications of the source code of the special functions [Press, Teukolsky, Vetterling, and Flannery (2002), Zhang and Jin (1996), Wolfram Research (2004)] in order to be evaluated to the sought precision. The results obtained by both C++ and Mathematica implementations agreed to all but the last two-three decimal digits in any desired precision.

3.1 Assembly and Solvability of the System

The most computationally demanding part of our approach is the assembly of the linear system the solution of which provides the expansion coefficients. This is because the L^2 norm minimization approach needs expensive 2D quadratures and apart from that all the entries of the matrix and right hand side vector involve special function evaluations which has to converge to the working precision. Moreover, the aforementioned systems involve extremely ill-conditioned matrices with condition numbers ranging from 10^{10} to 10^{160} and more, as it will be demonstrated in the sequel.

The solution of the linear systems was provided by Singular Value Decomposition (SVD) [Golub and Loan (1996), Press, Teukolsky, Vetterling, and Flannery (2002)] which allows direct calculation of the condition number of the matrices involved. As the most computationally intensive part of our approach was the assembly of the linear system and not its solution, in contrast to classical numerical methods, computational overhead associated with the specific choice of SVD over the classical LU decomposition was negligible.

In the scattering process under investigation we consider a spheroidal scatterer with large semi axis whose reduced length is kept constant and equal to one, while the small semi axis suitably varies to give birth to several aspect ratios. The excitation of the scattering mechanism has been accomplished with a plane wave corresponding to the wavenumber propagation vector $\mathbf{k} = k_x \hat{\mathbf{x}} + k_y \hat{\mathbf{y}} + k_z \hat{\mathbf{z}}$ where $k_x = k_y = k_z$, wavenumber increment $\delta k_i = 0.5\sqrt{3}$ and $k \in \{0.5\sqrt{3} - 4\sqrt{3}\}$ (all in reduced units). We have selected to apply an in-

cident wave field of this form to handle a rather generic excitation case. This increases the complexity of the numerical calculations involved, compared with the one coordinate axis oriented stimulation, but reveals the reliability and robustness of the adopted methodology in the general propagation case.

We should point out that the dimensionless product of the incident wavenumber k and the characteristic dimension of the prolate spheroid, taken as the large semi axis C , is being expanded beyond low frequency $kC \ll 1$ or resonance region $kC \simeq 1$. The range for the dimensionless product is taken from $kC = 0.5\sqrt{3}$ to $kC = 4\sqrt{3}$ in all our “computer” scattering “experiments”.

3.2 Condition Number

In Fig. 1 we plot the condition number of matrices arising from adopted methodology, as a function of the truncation level of the series N at various wavenumbers for a semi axes ratio equal to 0.6. It is evident that the condition number, is established mainly by the truncation level of the series while the role of the wavenumber of the incident field is almost negligible especially for values beyond $k = 0.5\sqrt{3}$. The linear dependence of the logarithm of the condition number $\kappa(A)$ on the truncation level N , presented in logarithmic scale in Fig. 1, reveals that the growth of the condition number with increasing N is clearly exponential. On the contrary the dependence of the condition number on the wavenumber k is hardly noticeable as the wavenumber increases from $k = 1\sqrt{3}$ up to $k = 4\sqrt{3}$.

In Fig. 2 we plot the condition number of the matrices for a truncation level of the series $N = 16$ as a function of the wavenumber k for several aspect-ratios of the scatterer, ranging from $a_R = 0.6$ to $a_R = 0.9$. For the low wavenumber region defined in $k \in [0.5\sqrt{3} - 1.5\sqrt{3}]$ there is an exponential decay with two different slopes in logarithmic representation for $k \in [0.5\sqrt{3} - 1\sqrt{3}]$ and from $k \in [1\sqrt{3} - 1.5\sqrt{3}]$. Surprisingly a plateau value for the condition number is being established for all the aspect ratios and the wavenumbers beyond $k = 1.5\sqrt{3}$. The conditioning of the system strongly depends on the truncation of the

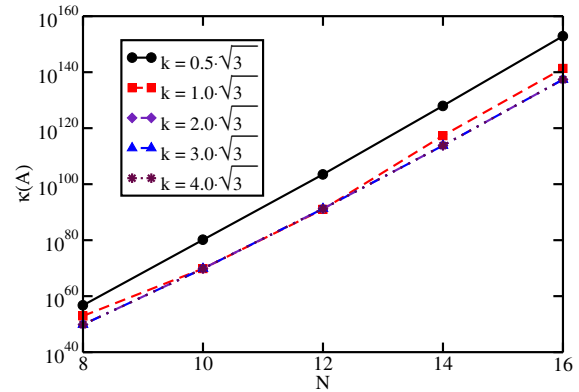


Figure 1: Condition number as a function of N for several k 's at $a_R = 0.6$.

series and not the geometry under investigation or the wavenumber of the incident wave.

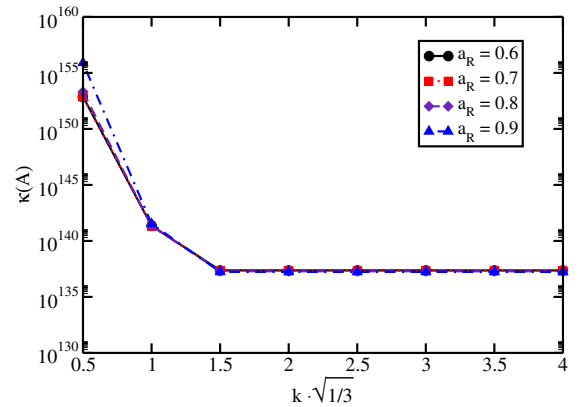


Figure 2: Condition number as a function of wavenumber k for several a_R 's at truncation level $N = 16$.

Due to the fact that those linear systems are highly ill-conditioned, the solution obtained by one back substitution is extremely inaccurate for the level of the working precision, as we can see in Table 1. To adjust the solution to our working precision we used iterative refinement [Golub and Loan (1996), Press, Teukolsky, Vetterling, and Flannery (2002)]. Error and residual bounds involved

in iterative refinement procedure, are adjusted to the working precision. Below, the desired precision was set to 170 decimal digits and the update ($\|dx\|_2$) and residual ($\|r\|_2$) Euclidean norm tolerances were adjusted to 10^{-170} and 10^{-172} respectively. As a rule of thumb the working precision

Table 1: Update and residual norms during iterative refinement.

Iteration	$\ dx\ _2$	$\ r\ _2$
1	1.213932e+14	7.060036e-60
2	5.556136e-18	9.824089e-127
3	7.734852e-85	3.159688e-133
4	2.130082e-164	3.159688e-133
5	1.831668e-166	3.159688e-133

should be tuned [Trefethen and Bau (1997)] to $\log_{10} \kappa(A)$. It is evident that in the first step of iterative refinement the norm of the solution update is still too large and five steps of iterative refinement need to be performed in order to reduce the Euclidean norm of the error to our working precision. The computational cost of iterative refinement procedure is negligible compared to that of the factorization of the matrix. This suggest that iterative refinement is a cheap way of obtaining highly accurate results when those are desirable.

3.3 Convergence Analysis

Our convergence study focuses on the treatment of boundary condition satisfaction (10). The convergence of the numerical solution to the solution of the exact scattering problem, is guaranteed by the establishment of the convergence of the error of the boundary condition satisfaction due to the well-posedness of the direct scattering problem.

In what follows we present an extensive study of the convergence in L^2 norm of the so constructed error function defined as

$$\|\varepsilon_N\|_{L^2(S)} = \left(\int_S |\varepsilon_N(\theta, \phi)|^2 dS \right)^{\frac{1}{2}},$$

$$\varepsilon_N(\theta, \phi) = (u_N^{sc}(\mathbf{r}) + u^{inc}(\mathbf{r}))|_{\mathbf{r} \in S} =$$

$$\sum_{n=0}^N \sum_{m=-n}^n A_{nm} \hat{u}_{nm}(\mu_0, \theta, \phi) + e^{i\mathbf{k} \cdot \mathbf{r}(\mu_0, \theta, \phi)}. \quad (14)$$

Computation of the integrals related to the L^2 norm was performed using Gauss-Legendre quadrature [Press, Teukolsky, Vetterling, and Flannery (2002)]. The number of the required quadrature points was adjusted such that the L^2 norm of the error converges to the fifth significant digit. The way several parameters of our physical problem, like the aspect ratio of the prolate spheroidal scatterer and the frequency of the incident field influence convergence, is exposed in the plots that follow. The convergence study is supplemented with 3D plots of the distribution of the real and imaginary parts of the error on the scatterer's surface. Figs. 3, 4, 5 and 6 plot

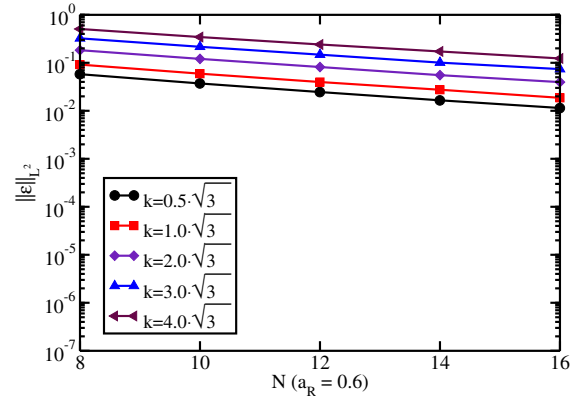


Figure 3: $\|\varepsilon\|_{L^2(S)}$ as a function of the truncation level N , $a_R = 0.6$, $k = 0.5\sqrt{3}, 1\sqrt{3}, 2\sqrt{3}, 3\sqrt{3}, 4\sqrt{3}$.

the dependence of the $\|\varepsilon_N\|_{L^2(S)}$ as a function of the truncation level of the series N for several wavenumbers ($k = 0.5\sqrt{3}, 1\sqrt{3}, 2\sqrt{3}, 3\sqrt{3}, 4\sqrt{3}$) of the incident wave, for each one of the scatterers ($a_R = 0.6, 0.7, 0.8, 0.9$) under consideration. The scale on the y axis is logarithmic.

Several interesting properties regarding the convergence of our approach emerge from those plots. First of all, we observe that in all the cases, the convergence is clearly exponential. For each scatterer, the error increases by increasing wavenumber (consequently frequency), but the convergence rate remains the same independently of the frequency. This is a very nice property

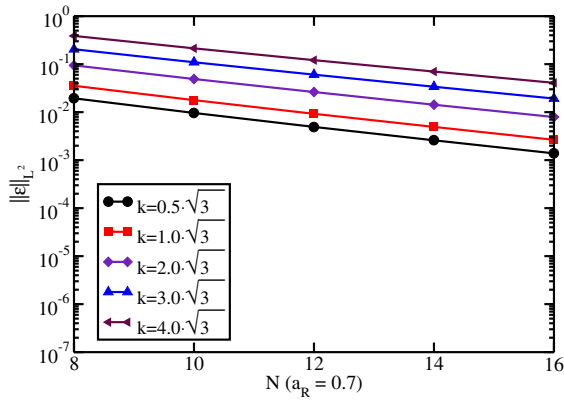


Figure 4: $\|\varepsilon\|_{L^2(S)}$ as a function of the truncation level N , $a_R = 0.7$, $k = 0.5\sqrt{3}, 1\sqrt{3}, 2\sqrt{3}, 3\sqrt{3}, 4\sqrt{3}$.

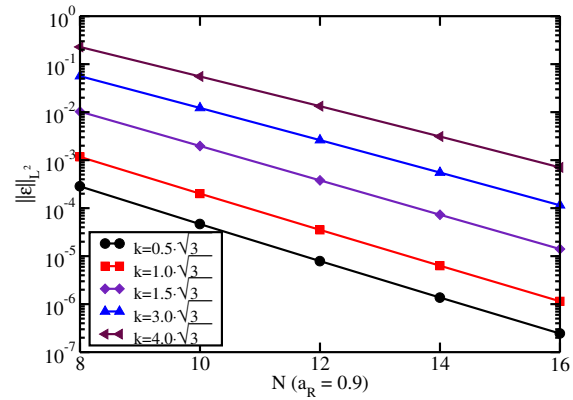


Figure 6: $\|\varepsilon\|_{L^2(S)}$ as a function of the truncation level N , $a_R = 0.9$, $k = 0.5\sqrt{3}, 1\sqrt{3}, 2\sqrt{3}, 3\sqrt{3}, 4\sqrt{3}$.

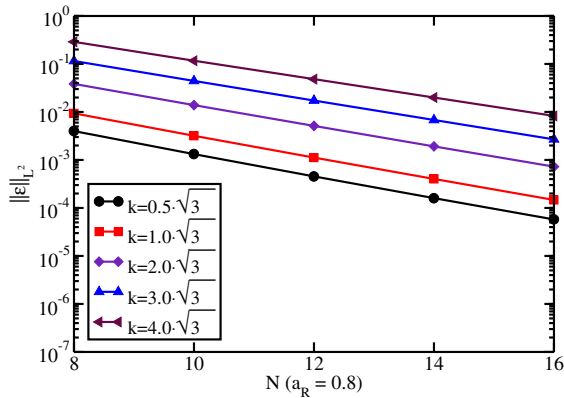


Figure 5: $\|\varepsilon\|_{L^2(S)}$ as a function of the truncation level N , $a_R = 0.8$, $k = 0.5\sqrt{3}, 1\sqrt{3}, 2\sqrt{3}, 3\sqrt{3}, 4\sqrt{3}$.

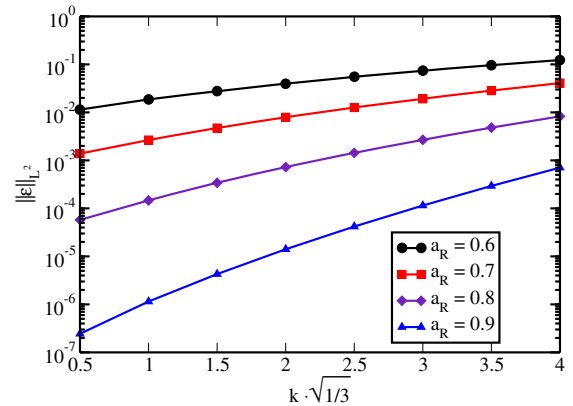


Figure 7: $\|\varepsilon\|_{L^2}$ as a function of wavenumber for various aspect ratios at truncation level 16.

which suggests that incident waves of high frequencies can be sufficiently handled by the current approach, if the convergence rate for the specific scatterer is sufficiently high. We observe however, that the convergence rate is strongly influenced by the aspect ratio of the spheroidal scatterer. The more elongated our spheroid becomes, the slower the series convergences. In Fig. 7 we plot again in logarithmic scale on the y axis the $\|\varepsilon_N\|_{L^2(S)}$ but now as a function of the wavenumber k for the aspect ratios under consideration

$a_R \in \{0.6, 0.7, 0.8, 0.9\}$ at $N = 16$. This plot reveals two important properties. As before convergence rate clearly deteriorates with smaller aspect ratios. The error exponentially increases with increasing wavenumber k .

The error dependence on the truncation level of the series N and on the aspect ratio a_R as depicted in Figs. 3, 4, 5, 6 and Fig. 7 allows a straight forward regression analysis which will hopefully express in a closed form, the L^2 norm of the error as a function of the three parameters involved, which

are the truncation level N , the aspect ratio a_R and the wavenumber k . This process is described below and involves the following three steps.

At the first, the dependence of the logarithm of the L^2 norm of the error, which is clearly linear with respect to the truncation level of the series N , is expressed as

$$\ln(\|\varepsilon\|_{L^2}(N, a_R, k)) = C(a_R, k)N + D(a_R, k) \quad (15)$$

where $C(a_R, k), D(a_R, k)$ are functions depending on the aspect ratio of the scatterer a_R and the wavenumber k . The values of $C(a_R, k), D(a_R, k)$ for different aspect ratios and for indicative wavenumbers k are summarized in Table (2) as they are obtained from regression analysis with correlation coefficients 0.999. Having calculated

Table 2: $C(a_R, k)$ and $D(a_R, k)$

a_R	k	$C(a_R, k)$	$D(a_R, k)$
0.60	$0.5\sqrt{3}$	-0.2023	-1.2552
	$1\sqrt{3}$	-0.1981	-0.8257
	$2\sqrt{3}$	-0.1920	-0.1828
	$3\sqrt{3}$	-0.1856	0.3331
	$4\sqrt{3}$	-0.1757	0.7056
0.70	$0.5\sqrt{3}$	-0.3299	-1.3274
	$1\sqrt{3}$	-0.3234	-0.7779
	$2\sqrt{3}$	-0.3096	0.0955
	$3\sqrt{3}$	-0.2951	0.7540
	$4\sqrt{3}$	-0.2809	1.2801
0.80	$0.5\sqrt{3}$	-0.5296	-1.3128
	$1\sqrt{3}$	-0.5191	-0.5413
	$2\sqrt{3}$	-0.4961	0.6951
	$3\sqrt{3}$	-0.4696	1.5875
	$4\sqrt{3}$	-0.4435	2.2968
0.90	$0.5\sqrt{3}$	-0.8822	-1.1351
	$1\sqrt{3}$	-0.8658	0.1568
	$2\sqrt{3}$	-0.8241	2.0133
	$3\sqrt{3}$	-0.7745	3.3340
	$4\sqrt{3}$	-0.7218	4.3189

the slope-regression coefficient $C(a_R, k)$ and the intercept-regression constant $D(a_R, k)$ we proceed

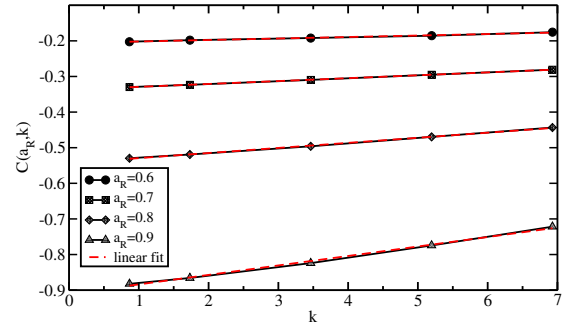


Figure 8: $C(a_R, k)$ as a function of wavenumber k for various aspect ratios a_R with the linear fit.

with the investigation of the dependence of slope and intercept as functions of the wavenumber k .

The dependence of $C(a_R, k)$, as can be seen in Fig. 8, is linear with respect to the wavenumber k and can be expressed as

$$C(a_R, k) = c_1(a_R)k + c_2(a_R), \quad (16)$$

where $c_1(a_R), c_2(a_R)$, depend only on the aspect ratio a_R . Values of the regression analysis for $c_1(a_R)$ and $c_2(a_R)$ are presented in Table (3). Then we try to describe the dependence of

Table 3: $c_1(a_R)$ and $c_2(a_R)$

a_R	$c_1(a_R)$	$c_2(a_R)$
0.6	0.0042	-0.2060
0.7	0.0081	-0.3373
0.8	0.0143	-0.5435
0.9	0.0266	-0.9104

$c_1(a_R), c_2(a_R)$ on the aspect ratio a_R by the following formulas

$$c_i(a_R) = c_{i0} + c_{i1}a_R + c_{i2}a_R^2 \quad (i = 1, 2), \quad (17)$$

using the computed values in Table 3. The parameters which best describe that dependence, where found to be $c_{10} = 0.0742, c_{11} = -0.2429, c_{12} = 0.2108$ with correlation coefficient 0.9987 and R.M.S per cent 0.0477 and $c_{20} = -2.0016, c_{21} =$

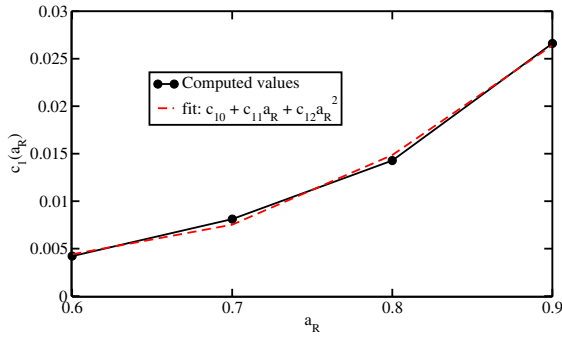


Figure 9: $c_1(a_R)$ in conjunction with the fitting function.

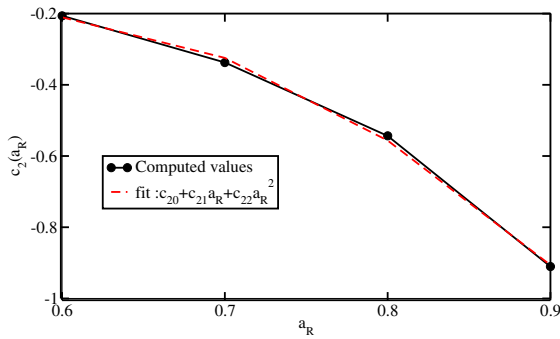


Figure 10: $c_2(a_R)$ in conjunction with the fitting function.

6.5219, $c_{22} = -5.8943$ with correlation coefficient 0.9994 and R.M.S. per cent 0.0248. Plots of the adjusted curves with the computed values for $c_1(a_R)$ and $c_2(a_R)$ are presented in Figs. 9, 10. It should be noted at this point, that every non-linear curve fitting has been made by adjusting the tolerance to 10^{-5} with an iterative process consisting of 500 iterative steps. We have followed a similar three step procedure for the decomposition of $D(a_R, k)$ venturing to find the best fitting functions. The intercept $D(a_R, k)$ plotted in Fig. 11, was expressed as a function of wavenumber k by the following formula

$$D(a_R, k) = d_1(a_R)\sqrt{k} + d_2(a_R). \tag{18}$$

The values of the non-linear curve fit are presented in Table 4. For the individual functions

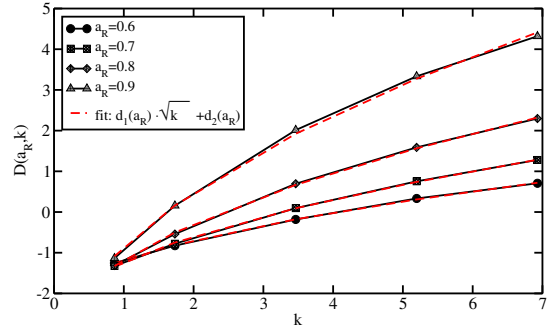


Figure 11: $D(a_R, k)$ for various aspect ratios a_R with the fitting function.

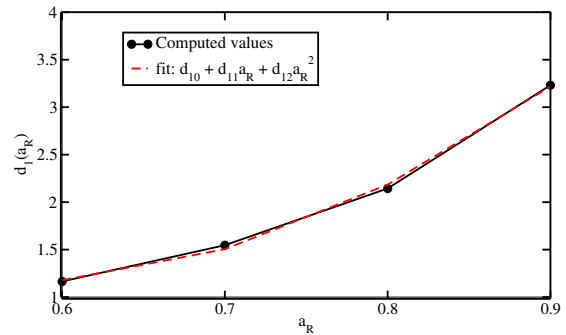


Figure 12: $d_1(a_R)$ (black) and fitting function (red dashed).

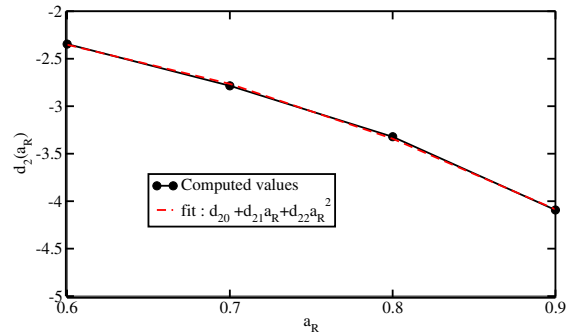


Figure 13: $d_2(a_R)$ (black) and fitting function (red dashed).

$d_1(a_R)$ and $d_2(a_R)$ we use the following fitting formulas

Table 4: Values of $d_1(a_R)$, $d_2(a_R)$, Correlation Coefficient (C.C.) Root Mean Square per cent of the Error (R.M.S.)

a_R	$d_1(a_R)$	$d_2(a_R)$	C.C.	R.M.S. (%) error
0.6	1.1645	-2.3456	0.9998	0.0362
0.7	1.5464	-2.7846	0.9999	0.0215
0.8	2.1437	-3.3221	0.9998	0.0389
0.9	3.2320	-4.0927	0.9994	0.0330

$$d_i(a_R) = d_{i0} + d_{i1}a_R + d_{i2}a_R^2 \quad i = 1, 2 \quad (19)$$

with the fitted values of the parameters involved being $d_{10} = 6.6344$, $d_{11} = -19.6893$, $d_{12} = 17.6595$ with correlation coefficient 0.9992 and R.M.S per cent 0.0176 and $d_{20} = -3.3617$, $d_{21} = 6.656$, $d_{22} = 8.2898$ with correlation coefficient 0.9997 and R.M.S. per cent 0.005. Figures 12, 13 are shown graphical representations of $d_1(a_R)$ and $d_2(a_R)$.

Additionally we have calculated the L^∞ norm defined by

$$\begin{aligned} \|\varepsilon_N\|_{L^\infty(S)} &= \left(\operatorname{ess\,sup}_S |\varepsilon_N| \right) \\ &= \max_S |\varepsilon_N|. \end{aligned} \quad (20)$$

In Figs. 14, 15, 16 and 17, we plot both the real and imaginary parts of the error ε_N on the surface of the scatterer for $N = 16$, wavenumber $k = 4\sqrt{3}$ and aspect ratios $a_R = 0.6$ and $a_R = 0.9$ correspondingly. Those 3D plots provide a detailed description of the error distribution. We can see that the error attains its maximum value on the poles of the spheroidal scatterer where the curvature is high.

Finally in Table 5, we provide indicative values for different aspect ratios for the real and imaginary part of the L^∞ norm, as well as for the L^2 norm of the error.

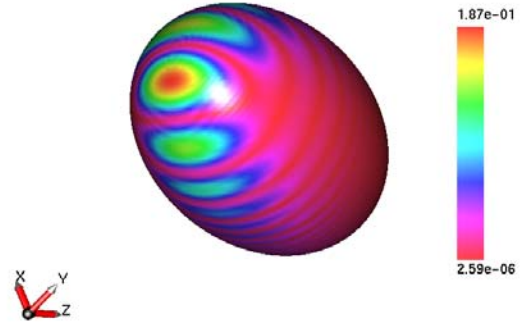


Figure 14: $Re(\varepsilon)$ at $a_R = 0.6$ and $k = 4\sqrt{3}$.

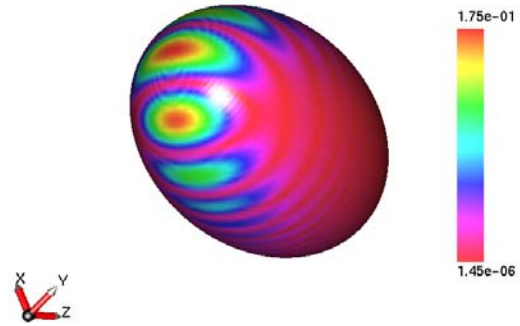


Figure 15: $Im(\varepsilon)$ at $a_R = 0.6$ and $k = 4\sqrt{3}$.

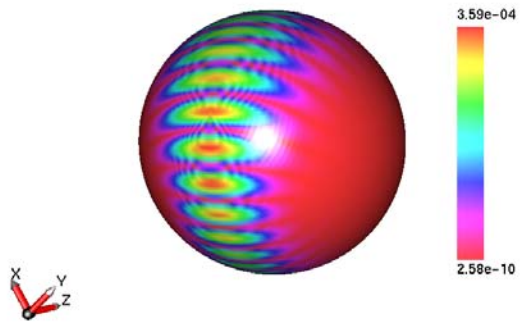


Figure 16: $Re(\varepsilon)$ at $a_R = 0.9$ and $k = 4\sqrt{3}$.

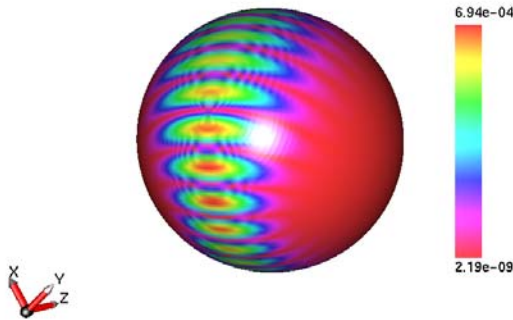


Figure 17: $Im(\epsilon)$ at $a_R = 0.9$ and $k = 4\sqrt{3}$.

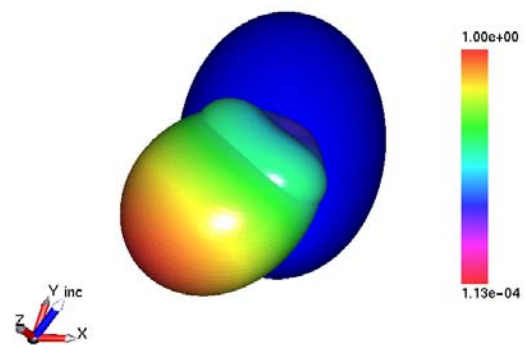


Figure 18: Far Field pattern (Re) for $a_R = 0.6$ at $k = 1.5\sqrt{3}$.

3.4 The Far Field Pattern

The far-field pattern constitutes the basic outcome of the analysis of the direct scattering problem. It is determined by Eq.(13), by substituting the calculated expansion coefficients provided by the preceding numerical process. In Figs.18-33 we visualize both the real and imaginary parts of the far-field pattern for the two extreme geometrical configurations $a_R = 0.6$, $a_R = 0.9$ and for wavenumbers starting from $k = 1.5\sqrt{3}$ since directivity becomes prominent from this specific value of the wavenumber. We have selected both real and imaginary parts, instead of the magnitude, to distinguish the two different contributions. Color bars give the quantitative description of the scattered field. The direction of the incident field is shown packed together with the axes system. Both the far field pattern and the scatterer are described on the same coordinate system and are rendered together to clarify the directionality of the scattered wave relative to the geometry of the scatterer.

Figs. 18-25 show the far field pattern obtained by the interaction of our incident field with the prolate spheroid of semi axes ratio $a_R = 0.6$. Usually for very low frequencies (wavenumber $k \approx 0.1$) the far field pattern exhibits an almost spherical shape, due to the fact that the incident field is not able (wavelength sensitivity) to follow the shape and curvature of the scatterer's surface. We observed this behavior by solving the forward scat-

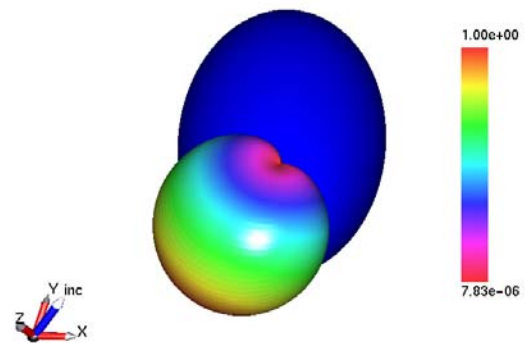


Figure 19: Far Field pattern (Im) for $a_R = 0.6$ at $k = 1.5\sqrt{3}$.

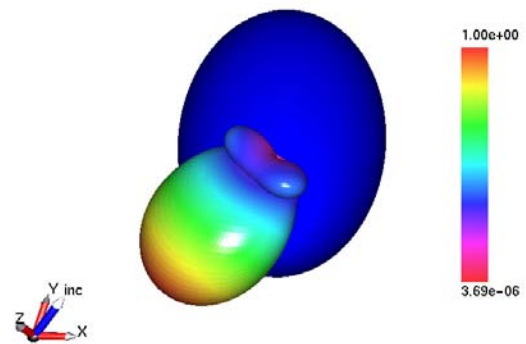


Figure 20: Far Field pattern (Re) for $a_R = 0.6$ at $k = 2\sqrt{3}$.

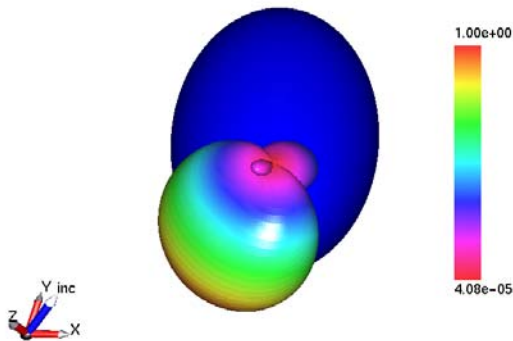


Figure 21: Far Field pattern (Im) for $a_R = 0.6$ at $k = 2\sqrt{3}$.

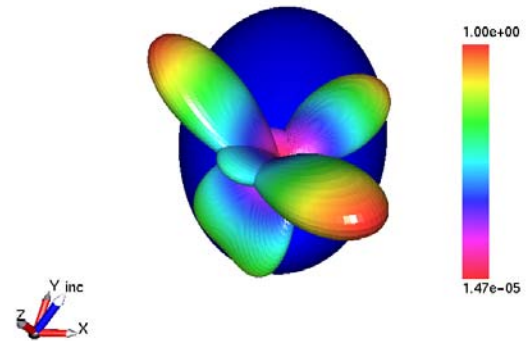


Figure 24: Far Field pattern (Re) for $a_R = 0.6$ at $k = 4\sqrt{3}$.

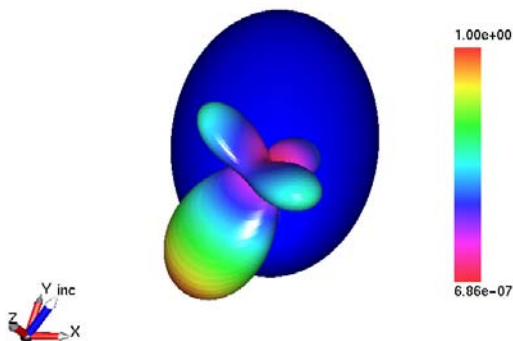


Figure 22: Far Field pattern (Re) for $a_R = 0.6$ at $k = 3\sqrt{3}$.

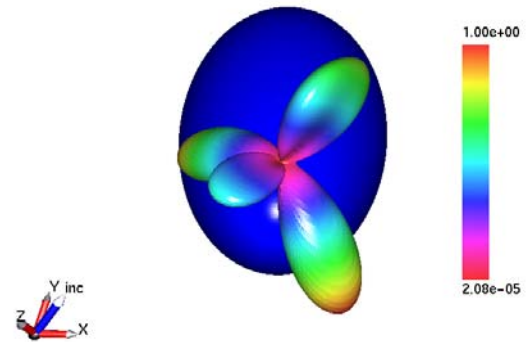


Figure 25: Far Field pattern (Im) for $a_R = 0.6$ at $k = 4\sqrt{3}$.

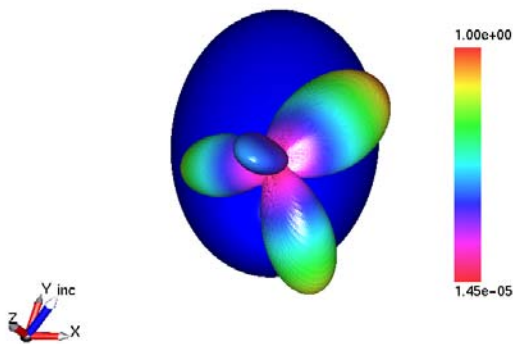


Figure 23: Far Field pattern (Im) for $a_R = 0.6$ at $k = 3\sqrt{3}$.

tering problem for wavenumbers around $k \approx 0.1$ (low frequency region). For this reason we begin, Figs.18, 19, with wavenumber $k = 1.5\sqrt{3}$ where we distinguish a single main lobe. In Figs. 20, 21 ($k = 2\sqrt{3}$), two individual secondary lobes emerge and grow in size as wavenumber increases. This procedure leads to exaggerated twin lobes for $k = 4\sqrt{3}$ indicating the redistribution of the scattering energy in particular favored directions. Directivity of the scattered field is observed for the imaginary part as well at different directions, suggesting that the total scattered field disposes a rich pattern of preferred scattering directions.

The case of semi axes ratio $a_R = 0.9$, is pre-

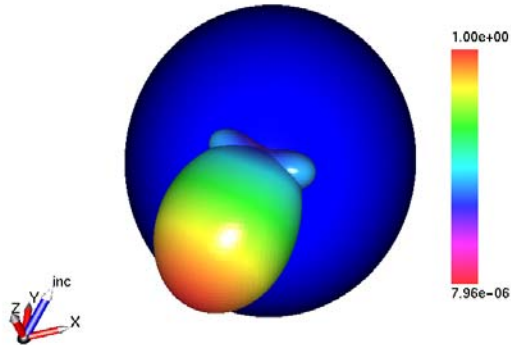


Figure 26: Far Field pattern (*Re*) for $a_R = 0.9$ at $k = 1.5\sqrt{3}$.

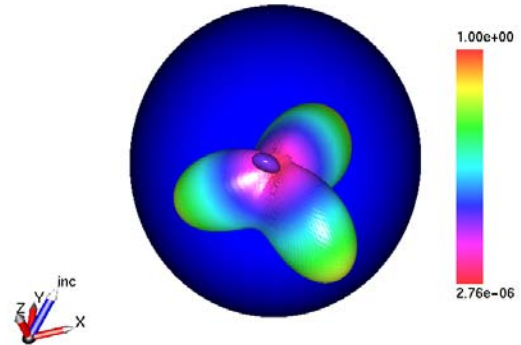


Figure 29: Far Field pattern (*Im*) for $a_R = 0.9$ at $k = 2\sqrt{3}$.

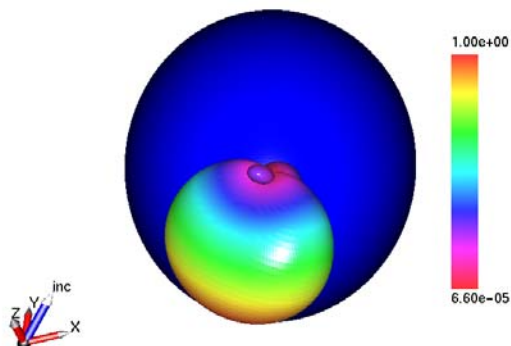


Figure 27: Far Field pattern (*Im*) for $a_R = 0.9$ at $k = 1.5\sqrt{3}$.

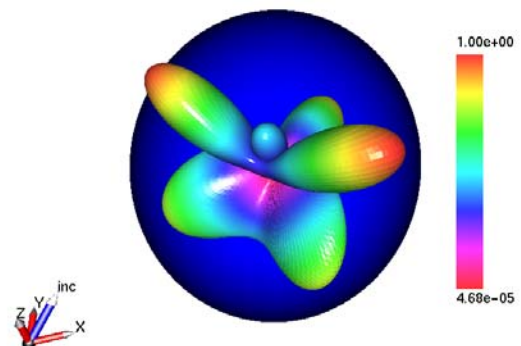


Figure 30: Far Field pattern (*Re*) for $a_R = 0.9$ at $k = 3\sqrt{3}$.

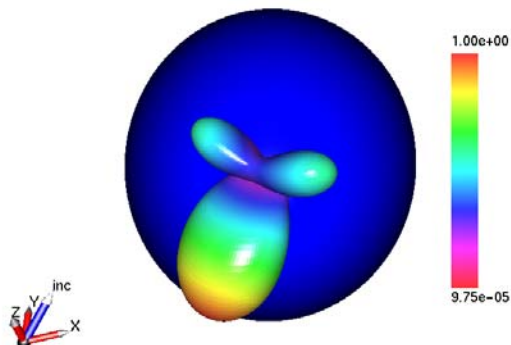


Figure 28: Far Field pattern (*Re*) for $a_R = 0.9$ at $k = 2\sqrt{3}$.

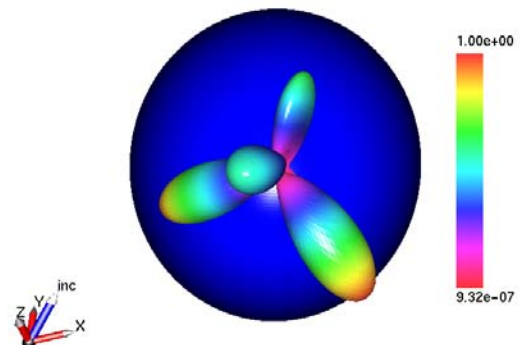


Figure 31: Far Field pattern (*Im*) for $a_R = 0.9$ at $k = 3\sqrt{3}$.

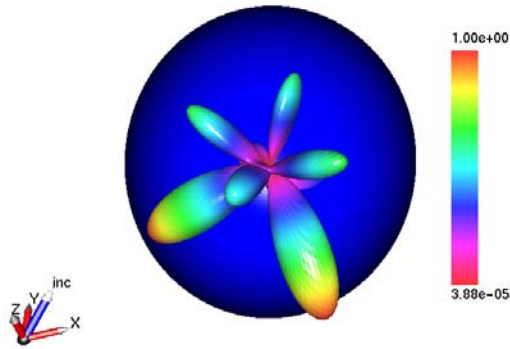


Figure 32: Far Field pattern (Re) for $a_R = 0.9$ at $k = 4\sqrt{3}$.

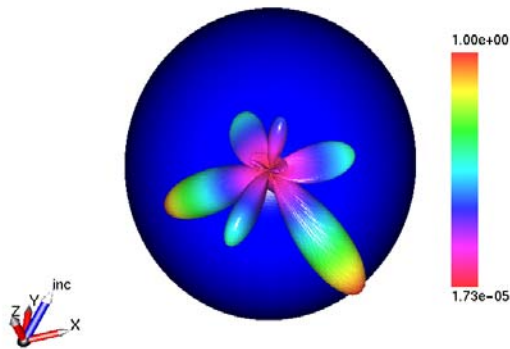


Figure 33: Far Field pattern (Im) for $a_R = 0.9$ at $k = 4\sqrt{3}$.

sented in Figs.26-33. Starting with wavenumber $k = 1.5\sqrt{3}$ we see as before, one main lobe both for the real and imaginary part of the far field pattern. As the frequency increases redistribution of energy occurs towards several favored directions which are more than those we observed in the previous case. This is clearly expected since for $a_R = 0.9$ the prolate spheroid is hardly distinguishable from a sphere ($a_R = 1.0$) which is not true for ($a_R = 0.6$) and generally more symmetries in geometrical configurations result in energy redistribution to more preferable directions.

Table 5: Error norms L^∞ and L^2 for truncation level $N=16$ as functions of the aspect ratio a_R and the dimensionless product kC of wave number and characteristic dimension of the scatterer. The latest being the large prolate spheroidal semi axis $C = 1$.

a_R	kC	$\ Re\{\varepsilon\}\ _{L^\infty}$	$\ Im\{\varepsilon\}\ _{L^\infty}$	$\ \varepsilon\ _{L^2}$
0.60	$0.5\sqrt{3}$	1.240e-2	2.636e-2	1.146e-2
	$1.0\sqrt{3}$	2.730e-2	3.755e-2	1.864e-2
	$1.5\sqrt{3}$	5.352e-2	4.109e-2	2.773e-2
	$2.0\sqrt{3}$	7.019e-2	6.129e-2	3.966e-2
	$2.5\sqrt{3}$	8.042e-2	9.740e-2	5.510e-2
	$3.0\sqrt{3}$	1.031e-1	1.267e-1	7.393e-2
	$3.5\sqrt{3}$	1.472e-1	1.483e-1	9.637e-2
	$4.0\sqrt{3}$	1.865e-1	1.749e-1	1.234e-1
0.70	$0.5\sqrt{3}$	1.256e-3	3.018e-3	1.386e-3
	$1.0\sqrt{3}$	4.022e-3	4.615e-3	2.656e-3
	$1.5\sqrt{3}$	7.508e-3	6.585e-3	4.718e-3
	$2.0\sqrt{3}$	1.076e-2	1.264e-2	7.917e-3
	$2.5\sqrt{3}$	1.516e-2	1.995e-2	1.263e-2
	$3.0\sqrt{3}$	2.477e-2	2.806e-2	1.923e-2
	$3.5\sqrt{3}$	3.599e-2	3.836e-2	2.841e-2
	$4.0\sqrt{3}$	4.884e-2	5.549e-2	4.083e-2
0.80	$0.5\sqrt{3}$	4.647e-5	1.118e-4	5.766e-5
	$1.0\sqrt{3}$	1.881e-4	2.176e-4	1.470e-4
	$1.5\sqrt{3}$	3.810e-4	4.946e-4	3.418e-4
	$2.0\sqrt{3}$	7.020e-4	1.033e-3	7.257e-4
	$2.5\sqrt{3}$	1.394e-3	1.895e-3	1.433e-3
	$3.0\sqrt{3}$	2.522e-3	3.340e-3	2.686e-3
	$3.5\sqrt{3}$	4.364e-3	5.815e-3	4.819e-3
	$4.0\sqrt{3}$	7.291e-3	9.734e-3	8.285e-3
0.90	$0.5\sqrt{3}$	1.847e-7	3.900e-7	2.440e-7
	$1.0\sqrt{3}$	8.354e-7	1.519e-6	1.147e-6
	$1.5\sqrt{3}$	2.599e-6	5.411e-6	4.280e-6
	$2.0\sqrt{3}$	8.332e-6	1.617e-5	1.409e-5
	$2.5\sqrt{3}$	2.317e-5	4.680e-5	4.184e-5
	$3.0\sqrt{3}$	6.031e-5	1.188e-4	1.149e-4
	$3.5\sqrt{3}$	1.520e-4	3.018e-4	2.936e-4
	$4.0\sqrt{3}$	3.589e-4	6.941e-4	7.069e-4

4 Conclusions

The purpose of this work is to study the sensitivity of the solution of the direct acoustic scattering problem in prolate spheroidal geometry with respect to the wavenumber and shape of the scatterer. We verified that one of the main issues when dealing with linear systems arising in those cases, is that we have to deal with extremely ill-

conditioned matrices. The corresponding linear systems cannot be solved with conventional 80-bit IEEE floating point arithmetic formats and integration of arbitrary precision software facilities is the only choice available. Iterative refinement can assist, in case arbitrary precision is integrated, in keeping the number of decimal digits required, as low as possible, improving in this way the performance. The suggested analytical method in conjunction with L^2 norm minimization of the error, related to the satisfaction of the boundary condition on the surface of the scatterer, proved to be a very robust technique which could accurately handle a wide range of elongated prolate spheroidal bodies and quite high frequencies (or equivalently the induced wavenumber) of the incident wave. Our convergence study revealed however, that for extremely elongated spheroidal bodies the convergence rate decreases. On the contrary, the frequency (wavenumber) of the incident field, does not affect the convergence rate but only increases the errors exponentially as it grows. This suggests that a solution to our problem for any frequency can be obtained, as long as the aspect ratio of the spheroid is such that it allows a relatively high convergence rate. The geometry of the scatterer, proved to be the most crucial parameter affecting the convergence. The specific dependence of the error on the geometrical, physical and numerical features of the problem has been revealed with detailed regression analysis.

Acknowledgement: Computations have been performed mainly in the Laboratory of Mathematical Modeling and Scientific Computing of the Materials Science Department using a Quad AMD Opteron. Additional computer resources were provided by the Research Center for Scientific Simulations (RCSS) of the University of Ioannina. For the 3D graphs we used the visualization software *OPSIS* created by the first author.

References

- Agnantiaris, J.; Polyzos, D.** (2003): A boundary element method for acoustic scattering from non-axisymmetric and axisymmetric elastic shells. *CMES: Computer Modeling in Engineering & Sciences*, vol. 4, pp. 197–212.
- Bailey, D. H.** (2004): High-precision floating-point arithmetic in scientific computation. *Lawrence Berkeley National Laboratory. Paper LBNL-57487. <http://repositories.cdlib.org/lbnl/LBNL-57487>.*
- Bailey, D. H.; Yozo, H.; Li, X. S.; Thompson, B.** (2002): Arprec: An arbitrary precision computation package. *Lawrence Berkeley National Laboratory. Paper LBNL-53651. <http://repositories.cdlib.org/lbnl/LBNL-53651>.*
- Borwein, J.; Bailey, D.** (2004): *Mathematics by Experiment, Plausible Reasoning in the 21st Century*. A.K. Peters.
- Callsen, S.; von Estorff, O.; Zaleski, O.** (2004): Direct and Indirect Approach of a Desingularized Boundary Element Formulation for Acoustical Problems. *CMES: Computer Modeling in Engineering & Sciences*, vol. 6, pp. 421–429.
- Chandler-Wilde, S.** (2007): Numerical methods for high frequency scattering problems. *Zurich Summer School*.
- Chandrasekhar, B.; Rao, M.** (2007): Acoustic Scattering from Fluid Bodies of Arbitrary Shape. *CMES: Computer Modeling in Engineering & Sciences*, vol. 21, pp. 67–80.
- Charalambopoulos, A.; Dassios, G.** (2002): On the vekua pair in spheroidal geometry and its role in solving boundary value problems. *Applicable Analysis*, vol. 81, pp. 85–113.
- Chen, H.; Fu, D. J.; Zhang, P.** (2007): An Investigation of Wave Propagation with High Wave Numbers via the Regularized LBIEM. *CMES: Computer Modeling in Engineering & Sciences*, vol. 20, pp. 85–98.
- Gergidis, L. N.; Kourounis, D.; Mavratzas, S.; Charalambopoulos, A.** (2007): Acoustic Scattering in Prolate Spheroidal Geometry via Vekua Transformation - Theory and Numerical results. *CMES: Computer Modeling in Engineering & Sciences*, vol. 21, pp. 157–175.

- Golub, G. H.; Loan, C. V.** (1996): *Matrix Computations*. The Johns Hopkins University Press, 3 edition.
- Hackman, R.** (1984): The transition matrix for acoustic and elastic wave scattering in prolate spheroidal coordinates. *J. Acoust. Soc. Am.*, vol. 75, pp. 35–45.
- He, Y.; Xie, Z.; Ye, Q.** (1997): Radiation and scattering of sound waves by a screened prolate spheroid. *Wave motion*, vol. 26, pp. 85–96.
- Press, W.; Teukolsky, S.; Vetterling, W.; Flannery, B.** (2002): *Numerical Recipes in C++*. Cambridge University Press, 2nd edition.
- Qian, Z.; Han, Z.; Atluri, S.** (2004): Directly derived non-hyper-singular boundary integral equations for acoustic problems, and their solution through Petrov-Galerkin schemes. *CMES: Computer Modeling in Engineering & Sciences*, vol. 5, pp. 541–562.
- Qian, Z.; Han, Z.; Ufimtsev, P.; Atluri, S.** (2004): Non-hyper-singular boundary integral equations for acoustic problems, implemented by the collocation-based boundary element method. *CMES: Computer Modeling in Engineering & Sciences*, vol. 6, pp. 133–144.
- Shewchuk, R.** (1997): Adaptive Precision Floating-Point Arithmetic and Fast Robust Geometric Predicates. *Discrete & Computational Geometry*, vol. 18, pp. 305–363.
- Trefethen, L. N.; Bau, D.** (1997): *Numerical Linear Algebra*. siam.
- Tsai, C.; Lin, Y.; Young, D.; Atluri, S.** (2006): Investigations on the accuracy and condition number for the method of fundamental solutions. *CMES: Computer Modeling in Engineering & Sciences*, vol. 16, pp. 103–114.
- Varadan, V.; Varadan, V.** (1982): Computation of rigid body scattering by prolate spheroids using the t-matrix approach. *J. Acoust. Soc. Am.*, vol. 71, pp. 22–25.
- Vekua, I.** (1942): Solutions of the equation $\Delta u + \lambda^2 u = 0$. *Soobshcheniya Akademii Nauk Gruz. SSSR*, vol. 3, pp. 307–314.
- Vekua, I.** (1945): Inversion of an integral transformation and some applications. *Soobshcheniya Akademii Nauk Gruz. SSSR*, vol. 6, pp. 177–183.
- Vekua, I.** (1967): *New Methods for Solving Elliptic Equations*. North Holland Publishing Co.
- Wang, H.; Wu, Q.; He, X.; Li, L.** (2005): Computation of wave scattering problems from spheric body: Derivation of the new sommerfeld-watson transformation. *Progress In Electromagnetics Research Symposium 2005, Hangzhou, China*, pp. 22–26.
- Waterman, P.** (1969): New formulation of acoustic scattering. *J. Acoust. Soc. Am.*, vol. 45, pp. 1417–1429.
- Wolfram Research, I.** (2004): *Mathematica Edition: Version 5.1*. Wolfram Research, Inc.
- Zhang, S.; Jin, J.** (1996): *Computation of Special functions*. Wiley Interscience.

